Journal of Sound and Vibration 333 (2014) 1079–1095

Contents lists available at ScienceDirect

Journal of Sound and Vibration

journal homepage: www.elsevier.com/locate/jsvi

Suppression of thermoelastic damping in MEMS beam resonators by piezoresistivity

X. Guo, Y.B. Yi *

Department of Mechanical and Materials Engineering, University of Denver, Colorado 80208, USA

ARTICLE INFO

Article history:
Received 4 March 2013
Received in revised form
23 September 2013
Accepted 28 September 2013
Handling Editor: A.V. Metrikine
Available online 30 October 2013

ABSTRACT

Microelectronic mechanical (MEM) beam resonators with high quality factors are always preferred in practical applications. As one of the damping sources, thermoelastic damping (TED) caused by irreversible heat flows is usually considered as an upper limit of the overall damping effect. A new method is proposed in this work to compensate TED by taking advantage of the piezoresistive effect. Such a method is implemented by applying an electrostatic field along the beam length with a negative piezoresistive coefficient. During a resonance, the stretched part of the beam generates a higher electrical power density and thus a higher temperature, while the compressed region leads to a lower temperature. Such a temperature distribution is opposite to the temperature change caused by the thermoelastic effect. The working principle is described by a set of coupled differential equations, which are subsequently solved by the finite element method. The result indicates that the TED in the beam resonators can be completely compensated when the strength of electrical field is tuned to a critical value, namely CEF. The value of the CEF is further analyzed by a series of parametric studies on various material properties and geometric factors.

1. Introduction

Silicon microelectronic mechanical (MEM) beam resonators are being developed aggressively for a variety of applications nowadays, such as sensing [1–3], time application and frequency controls [4,5] due to their advantages of high frequency and high quality factor. The miniaturized scale is also capable of batched fabrication for cost reduction. As one of the most important design characters, a high mechanical quality factor (i.e. Q-factor or Q-value) or less energy loss in a resonator means a better precision to operate as a sensor or a frequency filter. Therefore, it is of great importance to understand the dominating energy loss in the mechanical vibration to identify those factors that impose an upper limit of the Q-value and those factors that could be eliminated to improve the design. The dominant mechanisms from which the resonator dissipate energy include air damping, support loss [6,7] and thermoelastic damping (TED) [8–14]. Among them, air damping can be eliminated by packaging in vacuum because of the small size of the devices. But the support loss and TED can impose an upper limit on the design of micro resonators with high quality factors.

In vibrations of resonators, the non-equilibrium state of the temperature field is generated by the change of the strain field. Hence, the irreversible heat conduction between domains with different temperatures leads to the energy dissipation of TED. Zener [8,9] first studied TED in reeds and wires long time ago. However, the modern application of the theory to

* Corresponding author. Tel.: +1 3038712228.
E-mail address: yyi2@du.edu (Y.B. Yi).

0022-460X/$ - see front matter © 2013 Elsevier Ltd. All rights reserved.
http://dx.doi.org/10.1016/j.jsv.2013.09.041

micro/nanoelectronic mechanical systems should be attributed to Lifshitz and Roukes [10] whose work predicated the quality factor of TED for micro and nanobeam resonators based on thermal conduction along the height direction. By applying Green's function, Prabhakar and Srikar [11] analyzed TED by solving the two-dimensional heat transfer equation to obtain the thermoelastic temperature gradients along both the beam length and height simultaneously. The same research group [12] also analyzed the frequency shifts due to TED. Wong [13] presented an analytical solution for TED in a ring gyroscope based on Zener's method. However, these works were restricted to the flexural mode vibrations. Hao [14] derived the solution of quality factor for disk resonators vibrating in a contour mode by calculating the entropy increase per cycle of vibration. Sun [15,16] derived the analytical solution for out-of-plane vibrations of circular plate resonators through the thin plate theory in the cylindrical coordinates. In more complex conditions, TED under residual stresses is investigated by Zamanian [17] and Vahdat [18] for beam resonators. Kim [19] applied the simplified shell equations and utilized iterative schemes to analyze TED of nano-mechanical tube resonators with initial stresses. Tunvir [20] studied the nonlinear effect induced by a large vibration amplitude and found that there are opposite trends of the change in TED under adiabatic and isothermal surface thermal conditions. Vengallatore [21] and Prabhakar [22] presented an analytical solution to compute the frequency dependence of TED in bilayered beam resonators. In addition to the analytical methods, the finite element formulation [23–28] is a more efficient tool to determine the quality factor of TED for those systems with complex geometries [24–27] and mixed boundary conditions [28].

To enhance the quality factor, Pourkamali and Ayazi [29,30] utilized HARPSS process to decrease the gap between the MEMS resonator and the electrodes while TED still showed an upper limit to the total energy loss. Candler and Duwel [24] applied slot cuts in the beam resonator to disrupt the heat flow and then decrease TED based on both experimental work and numerical analysis, while a more comprehensive numerical study on TED and frequency shift in the beam with slot cuts was investigated by Guo et al. [27]. However, either the HARPSS method or adding slot cuts to the beam not only increases the fabrication cost, but also has a fabrication limit for nanoscale devices. Compared with these methods, utilizing the piezoresistive effect by applying an electrostatic field on the structure is a more flexible and cost-effective way to attenuate TED.

The current work is inspired by the research of Steeneken and Phan [31,32] who applied a direct voltage through a nanoscale silicon beam to generate self-sustained longitudinal vibration. They showed that the damping loss of vibration was fully compensated by the energy supplied by an electro-thermo-mechanical feedback in the system. In this paper, a similar energy supply mode by utilizing the piezoresistivity is applied to compensate TED in the flexural mode vibration. The mechanism is firstly explained by a series of differential equations for the couplings among the electrical, thermal and mechanical processes. Thereafter a set of finite element equations are derived and the quality factor is computed from an eigenvalue analysis.

2. Methods

As a key design parameter of resonators, the Q-value is used to describe the energy loss in each cycle of vibration. Less energy loss is preferred to maintain the vibration with higher amplitude or a sharper peak in the frequency response. The Q-value is defined as the following ratio:

$$Q = 2\pi \frac{W}{\Delta W} \tag{1}$$

where W is the maximum vibration energy stored in the system and ΔW is the energy dissipation over one cycle.

2.1. Physical mechanism

The energy loss due to the relaxation of mechanically induced temperature gradients and the resulting irreversible heat flow is show in Fig. 1. The compression in the beam leads to a higher temperature (hot) region while the tensile stress on the opposite side of the beam results in a lower temperature (cold) region. We assume that an electrostatic field is applied on

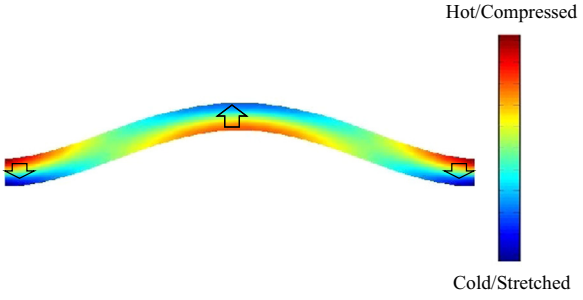

Fig. 1. Temperature contour plot of the clamped–clamped MEMS beam resonator in flexural vibration. The heat flow, illustrated by the arrows, is caused by the temperature gradient and contributes to TED.

a clamped–clamped silicon beam resonator. When the system starts to vibrate in a fashion shown in Fig. 1, the resistance R of the compressed region can be found as

$$R = R_0(1+\pi_l\sigma) \tag{2}$$

where R_0 is the resistance without the stress load. π_l and σ are the piezoresistive coefficient and the mechanical stress, respectively. The electrical power P generated is defined as

$$P = U^2/R \tag{3}$$

where U is the voltage across the compressed region. When the resonator has a negative piezoresistive coefficient, such as single crystal silicon after N-type doping, R will increase and P will decrease in those regions subjected to compressive stresses. Hence, the piezoresistive effect leads to a reduced electrical power and thus a lower temperature in the compressed region, whereas the temperature in the stretched region increases. Consequently the temperature gradient generated by the thermoelasic effect shown in Fig. 1 is attenuated by the reverse temperature gradient induced by the piezoresistivity. The reduced heat low rate results in a less energy loss and a higher quality factor. Briefly, the mechanism is closely related to the coupling among conductive heat transfer, mechanical vibration and electrical piezoresistive effect.

2.2. Heat transfer

The heat transfer equation involved in TED is known as

$$\rho c_p \frac{\partial T}{\partial t} - \nabla\cdot(k\nabla T) = P_m + P_e \tag{4}$$

where ρ is the density of the material, c_p is the specific heat capacity, T is the temperature, k is the thermal conductivity, P_m and P_e are the heat generation rate per unit volume caused by the thermoelastic deformation and the amplitude of the electrical power change, respectively. The heat generation P_m comes from thermoelastic heating governed by

$$P_m = -\frac{E\alpha T_a}{(1-\upsilon)}\frac{\partial \varepsilon}{\partial t} \tag{5}$$

where E is Young's modulus, α is the coefficient of thermal expansion, T_a is the ambient temperature, υ is Poisson's ratio, and the dilatation strain tensor $\boldsymbol{\varepsilon}$ is defined as

$$\boldsymbol{\varepsilon} = \nabla\cdot\mathbf{U} = \nabla\cdot(u_{11}+u_{22}+u_{33}) \tag{6}$$

where $\mathbf{U}$ is the displacement tensor; u_{11}, u_{22} and u_{33} are the strain components in the x-, y- and z-directions, respectively.

2.3. Mechanical vibration

In the theory of vibration, the equation of motion for an elastic solid is obtained from the following force equilibrium:

$$\rho\frac{\partial^2\mathbf{U}}{\partial^2 t^2} = \nabla\cdot\boldsymbol{\sigma} \tag{7}$$

where $\boldsymbol{\sigma}$ is the stress tensor. The stress under mechanical relaxation is defined by Hooke's Law:

$$\boldsymbol{\sigma} = C\boldsymbol{\varepsilon} = \mathbf{C}(\boldsymbol{\varepsilon}_\mathbf{s} - \boldsymbol{\varepsilon}_\mathbf{t}) = \mathbf{C}(\boldsymbol{\varepsilon}_\mathbf{s} - aT) \tag{8}$$

where $\mathbf{C}$ is the stiffness tensor, $\boldsymbol{\varepsilon}_\mathbf{s}$ is the strain tensor without thermal effect, and $\boldsymbol{\varepsilon}_\mathbf{t}$ is the thermal strain tensor.

2.4. Piezoresistive effect on electrical power

The continuity equation for the electrical current $\mathbf{J}$ under an electrostatic field $\mathbf{E}_\mathbf{e}$ can be written as

$$\nabla\cdot\mathbf{J} = \nabla\cdot\sigma_e\mathbf{E}_\mathbf{e} = 0 \tag{9}$$

where σ_e is the electrical conductivity.

The electrical power P_e can be found from

$$P_e = \mathbf{E}_\mathbf{e}\cdot\mathbf{J} = \sigma_e\mathbf{E}_\mathbf{e}^2 \tag{10}$$

In the present of piezoresistivity, the electrical conductivity, σ_e, is composed of two terms: the static component denoted by 's' and the harmonic component induced by the mechanical stress denoted by 'h'. Eq. (10) is then rewritten as

$$P_{eh} = (\sigma_{es}+\sigma_{eh})\mathbf{E}_\mathbf{e}^2 \tag{11}$$

where the harmonic component in the electrical power, P_{eh}, is defined as

$$P_{eh} = \sigma_{eh}\mathbf{E}_\mathbf{e}^2 \tag{12}$$

As indicated in Eq. (9), the electrostatic field $\mathbf{E_e}$ is obtained from

$$\nabla \cdot \sigma_{es}\mathbf{E_e} = 0 \tag{13}$$

The change in the conductivity σ_{eh} is defined by

$$\sigma_{eh} = \pi_l \frac{\boldsymbol{\sigma}}{\sigma_{es}} \tag{14}$$

where $\boldsymbol{\sigma}$ the mechanical stress aforementioned. The resistance R_0 in Eq. (2) is defined as

$$R_0 = \rho_{es}\frac{L}{A} = \frac{L}{\sigma_{es}A} \tag{15}$$

where ρ_{es} is the static electrical resistivity; L and A are the length and cross-sectional area of conductor, respectively. The harmonic component of the electrical resistivity ρ_{eh} in the matrix form due to the mechanical stress $\boldsymbol{\sigma}$ is defined by the following equation [33]:

$$\boldsymbol{\rho_{eh}} = \begin{bmatrix} \rho_{eh11} \\ \rho_{eh22} \\ \rho_{eh33} \\ \rho_{eh23} \\ \rho_{eh31} \\ \rho_{eh12} \end{bmatrix} = \rho_{es}\boldsymbol{\pi_{ij}}\boldsymbol{\sigma} = \rho_{es}\begin{bmatrix} \pi_{11} & \pi_{12} & \pi_{12} & 0 & 0 & 0 \\ \pi_{12} & \pi_{11} & \pi_{12} & 0 & 0 & 0 \\ \pi_{12} & \pi_{12} & \pi_{11} & 0 & 0 & 0 \\ 0 & 0 & 0 & \pi_{44} & 0 & 0 \\ 0 & 0 & 0 & 0 & \pi_{44} & 0 \\ 0 & 0 & 0 & 0 & 0 & \pi_{44} \end{bmatrix}\begin{bmatrix} \sigma_{11} \\ \sigma_{22} \\ \sigma_{33} \\ \sigma_{23} \\ \sigma_{31} \\ \sigma_{12} \end{bmatrix} \tag{16}$$

where $\boldsymbol{\pi_{ij}}$ is the piezoresistive tensor; σ_{11}, σ_{22} and σ_{33} are the stress components in the x-, y- and z-directions, respectively. The electrical conductivity, σ_e, is defined as

$$\sigma_e = 1/(\rho_{es} + \rho_{eh}) \tag{17}$$

which can be expressed as the following matrix form [31]

$$\boldsymbol{\sigma_e} = \boldsymbol{\sigma_{es}} + \boldsymbol{\sigma_{eh}} = \frac{1}{\rho_{es}}\begin{bmatrix} 1 & 0 & 0 \\ 0 & 1 & 0 \\ 0 & 0 & 1 \end{bmatrix} - \frac{1}{\rho_{es}^2}\begin{bmatrix} \rho_{eh11} & \rho_{eh12} & \rho_{eh31} \\ \rho_{eh12} & \rho_{eh22} & \rho_{eh23} \\ \rho_{eh31} & \rho_{eh23} & \rho_{eh33} \end{bmatrix} \tag{18}$$

For two-dimensional problems, Eqs. (16) and (18) degenerate to

$$\boldsymbol{\rho_{eh}} = \begin{bmatrix} \rho_{eh11} \\ \rho_{eh22} \\ \rho_{eh12} \end{bmatrix} = \rho_{es}\begin{bmatrix} \pi_{11} & \pi_{12} & 0 \\ \pi_{12} & \pi_{11} & 0 \\ 0 & 0 & \pi_{44} \end{bmatrix}\begin{bmatrix} \sigma_{11} \\ \sigma_{22} \\ \sigma_{12} \end{bmatrix} \tag{19}$$

and

$$\boldsymbol{\sigma_e} = \boldsymbol{\sigma_{es}} + \boldsymbol{\sigma_{eh}} = \frac{1}{\rho_{es}}\begin{bmatrix} 1 & 0 \\ 0 & 1 \end{bmatrix} - \frac{1}{\rho_{es}^2}\begin{bmatrix} \rho_{eh11} & \rho_{eh12} \\ \rho_{eh12} & \rho_{eh22} \end{bmatrix} \tag{20}$$

Therefore,

$$\boldsymbol{\sigma_{eh}} = -\frac{1}{\rho_{es}^2}\begin{bmatrix} \rho_{eh11} & \rho_{eh12} \\ \rho_{eh12} & \rho_{eh22} \end{bmatrix} \tag{21}$$

Substituting Eqs. (19)–(21) results in

$$\sigma_{\mathbf{eh}} = -\frac{1}{\rho_{es}}\begin{bmatrix} \pi_{11}\sigma_{11} + \pi_{12}\sigma_{22} & \pi_{44}\sigma_{12} \\ \pi_{44}\sigma_{12} & \pi_{12}\sigma_{11} + \pi_{11}\sigma_{22} \end{bmatrix} \tag{22}$$

2.5. Finite element formulations

In harmonic vibration, the temperature and displacement have the following forms

$$T = T_0 \mathrm{e}^{\mathrm{i}\omega t} \tag{23}$$

$$U = U_0 \mathrm{e}^{\mathrm{i}\omega t} \tag{24}$$

$$V = V_{\mathbf{0}} e^{\mathrm{i}\omega t} = \frac{\partial U}{\partial t}\mathrm{e}^{\mathrm{i}\omega t} = \mathrm{i}\omega V_{\mathbf{0}} e^{\mathrm{i}\omega t} \tag{25}$$

where ω is the angular frequency and generally complex when damping is present; V is the velocity; T_0, U_0, and V_0 are the amplitudes of temperature, displacement and velocity, respectively.

By applying the interpolating function N (i.e. the shape function) to Eqs. (4)–(6), we obtain the following finite element equations:

$$(\mathbf{K}+\omega\mathbf{H})T+\omega\mathbf{F}U+\mathbf{P_{eh}}=0 \tag{26}$$

where **K**, **H** and **F** are the coefficient matrices; T is the nodal temperature; U is the nodal displacement and $\mathbf{P_{eh}}$ is the harmonic electrical power change. The nodal strain is given by

$$\boldsymbol{\varepsilon}=BU=\nabla\cdot(NU) \tag{27}$$

where B is the strain–displacement function in finite element method.

Similarly, Eqs. (7) and (8) are converted into the following form using the same interpolating function,

$$\mathbf{L}U-\mathbf{G}T+\omega\mathbf{M}V=0 \tag{28}$$

where **L**, **G**, and **M** are the coefficient matrices, and V is the nodal velocity. In addition to Eqs. (26) and (28), one more equation is needed to solve for the three unknowns U, T and V. The third equation has already been shown in Eq. (25). That is

$$V=i\omega U \tag{29}$$

where the method to compute the coefficient matrices **K**, **H**, **F**, **L**, **G** and **M** has been described in Refs. [25,27].

The vector form of Eq. (12) can be expressed as

$$\mathbf{P_{eh}}=(\boldsymbol{\sigma}_{\mathbf{eh}}\mathbf{E_e})'\cdot\mathbf{E_e} \tag{30}$$

where $\mathbf{E_e}$ is obtained from Eq. (13) and

$$\mathbf{E_e}=\begin{bmatrix}E_{e11}\\E_{e22}\end{bmatrix} \tag{31}$$

Substituting Eqs. (22) and (31) into (30) yields

$$\mathbf{P_{eh}}=Y\boldsymbol{\sigma}=-\frac{1}{\rho_{es}}\begin{bmatrix}\pi_{11}E_{e11}^2+\pi_{12}E_{e22}^2\\ \pi_{12}E_{e11}^2+\pi_{11}E_{e22}^2\\ 2\pi_{44}E_{e11}E_{e22}\end{bmatrix}^{-1}\begin{bmatrix}\sigma_{11}\\\sigma_{22}\\\sigma_{12}\end{bmatrix} \tag{32}$$

Meanwhile substituting Eqs. (8) and (27) into (32) leads to

$$\mathbf{P_{eh}}=Y\boldsymbol{\sigma}=\mathrm{YC}\varepsilon=\mathrm{YCBU} \tag{33}$$

In an elemental domain,

$$\mathbf{P_{eh}}=\mathrm{SU} \tag{34}$$

where

$$\mathbf{S}=\iint\mathbf{N}^{\mathrm{T}}\mathbf{YCB}\,\mathrm{d}x\mathrm{d}y \tag{35}$$

2.6. Eigenvalue equations

Combining Eqs. (26), (28), (29) and (34) yields,

$$\begin{bmatrix}-\mathbf{K}&\mathbf{S}&0\\ \mathbf{G}&-\mathbf{L}&0\\ 0&0&\mathbf{I}\end{bmatrix}\begin{bmatrix}T\\U\\V\end{bmatrix}=\mathrm{i}\omega\begin{bmatrix}\mathbf{H}&\mathbf{F}&0\\ 0&0&\mathbf{M}\\ 0&\mathbf{I}&0\end{bmatrix}\begin{bmatrix}T\\U\\V\end{bmatrix} \tag{36}$$

where **I** is an identity matrix. This is a standard eigenvalue equation. The eigenvalue of the equation is the angular frequency ω (i.e. the eigenfrequency) whose corresponding eigenmode is denoted by the eigenvectors **U**, **V**, and **T**. When the electrical field is absent, S equals zero and Eq. (36) degenerates to the situation involving TED alone, which was already studied in Refs. [25,27]. By formulating the velocity field to be independent of the displacement, the originally quadratic Eq. (7) is reduced to two first-order equations, i.e. Eqs. (28) and (29).

The quality factor of the system can be evaluated from

$$Q=\frac{1}{2}\left|\frac{\mathrm{Re}(\omega)}{\mathrm{Im}(\omega)}\right| \tag{37}$$

where $\mathrm{Re}(\omega)$ is the real part of ω giving the angular frequency in the presence of both thermoelasticity and piezoresisitivity; $\mathrm{Im}(\omega)$ is the imaginary part of ω representing the attenuation of vibration. The finite element algorithm is developed in the form of a customized MATLAB code.

3. Results and discussions

3.1. Power change by piezoresistive effect

As discussed in the former section, TED can be compensated by the reduced temperature difference due to the change in the electrical power generation. Such a power change can be computed by Eq. (34) as a function of the displacement. A schematic of the electrical connection for providing the electrical field is shown in Fig. 2(a). To illustrate the temperature distribution by the piezoresistive effect, the power change in the silicon beam is computed when the driving force '*F*' is assumed constant. The result is shown in Fig. 2(b). The micro beam in the numerical analysis is assumed as single crystal silicon with length 200 μm, height 10 μm and thickness 20 μm. The voltage V_e applied across the silicon beam is 2 V. The center of the beam is exerted by a concentrated force $F=2\times10^{-10}$ (N), and both ends of the beam are clamped. The properties of the single crystal silicon after N-type doping (with a negative piezoresistive coefficient) are listed in Table 1. The analysis is performed in the two-dimensional plane strain condition. To minimize the computational effort, the model is simplified into a half beam by taking advantage of its geometric symmetry, as shown in Fig. 2(b).

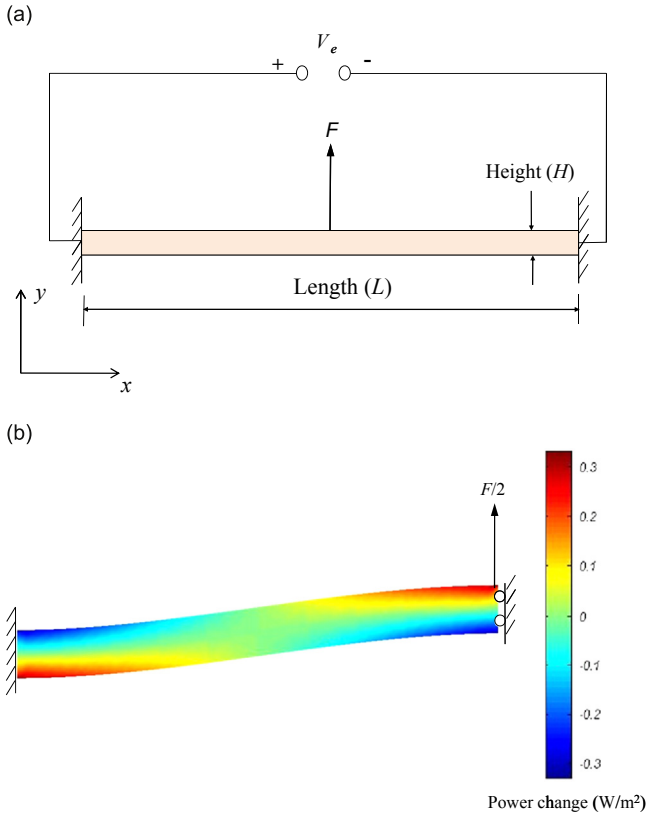

Fig. 2. (a) Schematic of the beam resonator under a central driving force with a static electrical field. (b) The simplified structure (half beam) with the distribution of the nodal power (W/m^2) under a constant central driving force.

Table 1
Material properties of single crystal silicon after N-type doping.

Young's modulus (Pa)	1.57×10^{11}
Poisson's ratio	0.22
Thermal expansion coefficient (K^{-1})	2.6×10^{-6}
Thermal conductivity ($W\,m^{-1}K^{-1}$)	90
Specific heat ($J\,kg^{-1}\,K^{-1}$)	700
Density ($kg\,m^{-3}$)	2330
Ambient temperature (K)	300
Piezoresistivity, $\pi_{11}/\pi_{12}/\pi_{44}$ (Pa^{-1})	$-102.2/53.4/-13.6\times10^{11}$
Static electrical resistivity (Ω m)	1×10^{-4}

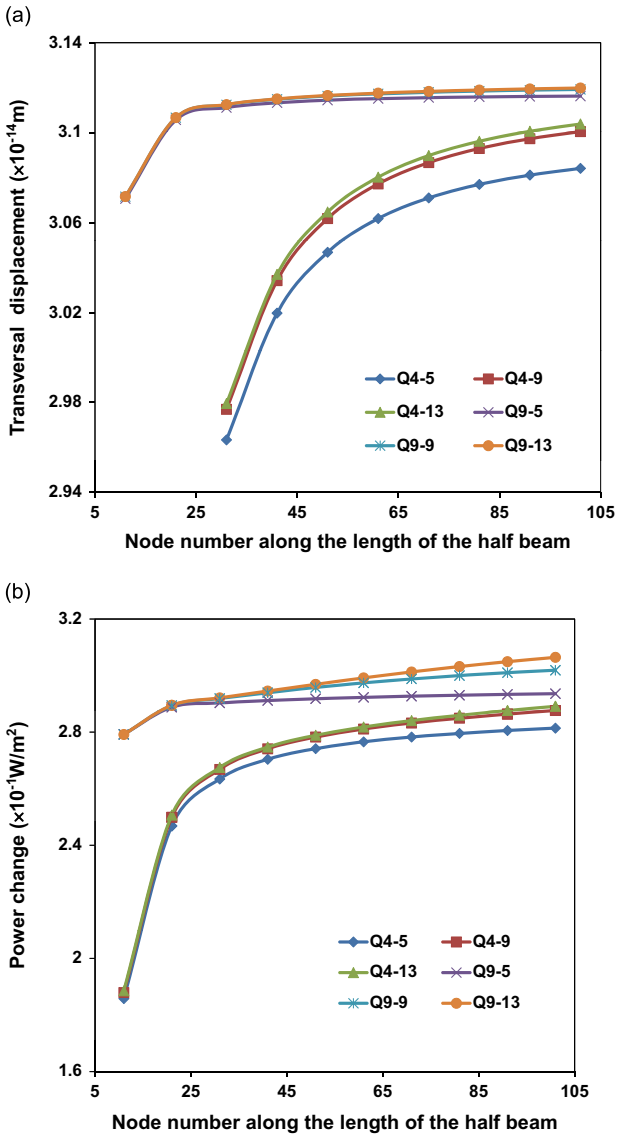

Fig. 3. Results of (a) the transverse displacement and (b) power change of the upright corner node (shown in Fig. 2(b)) in the convergence test.

The nodal strength of the electrical field was computed from either the finite element analysis for a complex geometry, or the equations $E_{e11}=V_e/L$ and $E_{e22}=0$ for a straight beam with uniform cross-section. It was followed by a stress-strain analysis for the nodal values of the displacements, stresses and strains. The result was then used to find the electrical power change directly from Eq. (34) or a combination of Eqs. (19), (21) and (30). It turns out that both the direct and the sequential methods lead to the same result, which can be considered as a validation of Eq. (34) despite the fact that the piezoresistive effect is anisotropic. The change in the nodal power is shown in Fig. 2(b) based on the 9-node quadrilateral (Q9) elements with 51 nodes along the length and 13 nodes along the height. It has been found that the distribution of power change leads to a reversed temperature gradient in comparison with that shown in Fig. 1.

Additionally the relationship between the results and the mesh density was studied by employing the 4-node linear quadrilateral (Q4) elements and Q9 elements with various node numbers. The results of the transversal displacement and the power change at the node where the force is exerted are shown in Fig. 3. The horizontal axis of Fig. 3 represents the number of nodes along the length of the half beam, while the number of nodes along the height is 5, 9 and 13. The result shows that the Q9 elements converge faster than the Q4 elements even when a coarse mesh is used with only 5 nodes (i.e. two Q9 elements) along the height and 21 nodes (i.e. ten Q9 elements) along the length. In addition, Fig. 3 shows that the results using 9 or 13 nodes along the height are quite close to each other, for both Q4 and Q9 element types.

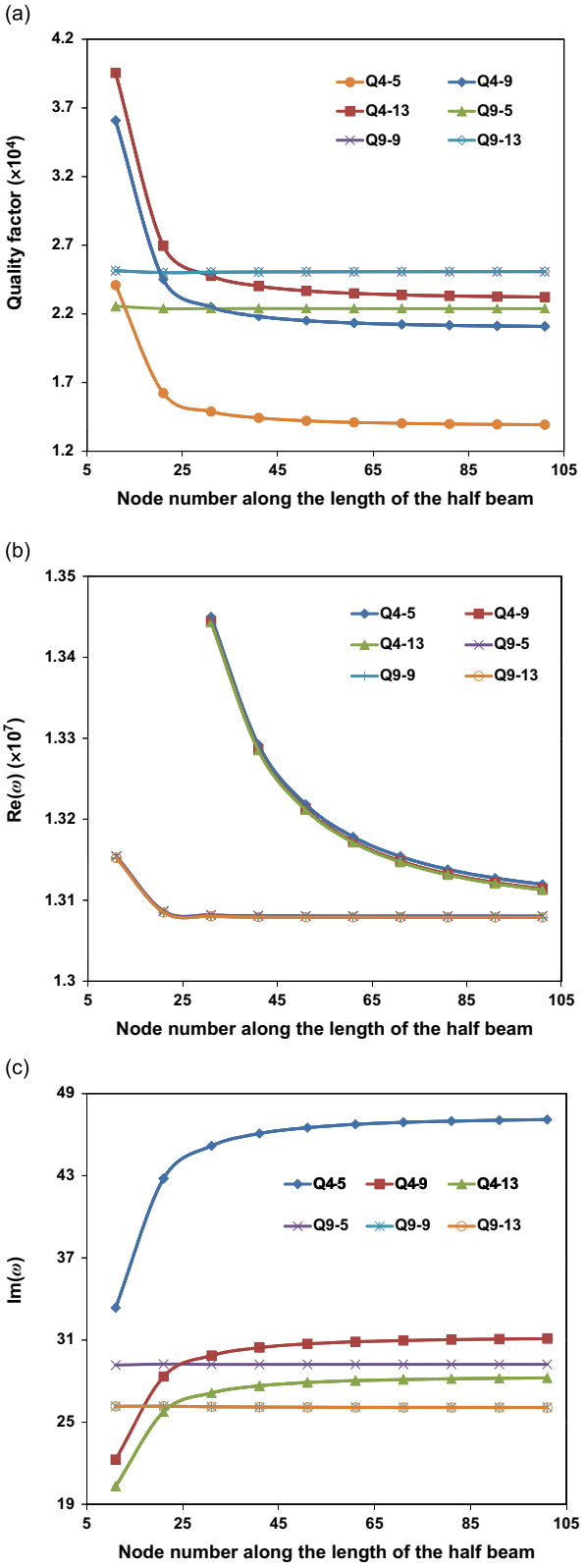

Fig. 4. Convergence test of (a) the quality factor, (b) Re(ω), and (c) Im(ω) using Q4 and Q9 elements with different mesh densities.

3.2. Convergence studies

The convergence studies on the quality factor along with Re(ω) and Im(ω) were also performed by using both Q4 and Q9 elements. When the electrical field is absent (i.e. $V_e=0$), the system degenerates to a standard TED problem and a number of analytical methods exist in the literature. In order to compare the numerical results of TED with the analytical results reported in Ref. [10], we set Poisson's ratio to zero. The geometry and material properties of the silicon beam remain the

Table 2
Results from the convergence studies.

V_e	Result	9×41 mesh	13×101 mesh	Error (%)*
0V	Q	14,723.65	14,721.06	0.0176
	Im(ω)	444.156	444.215	−0.0133
	Re(ω)	13,079,200	13,078,640	0.00428
2V	Q	250,470.9	250,866.6	−0.158
	Im(ω)	26.10957	26.06727	0.162
	Re(ω)	13,079,380	13,078,810	0.00436

* The error is estimated by comparing the result of 9×41 with that of 13×101.

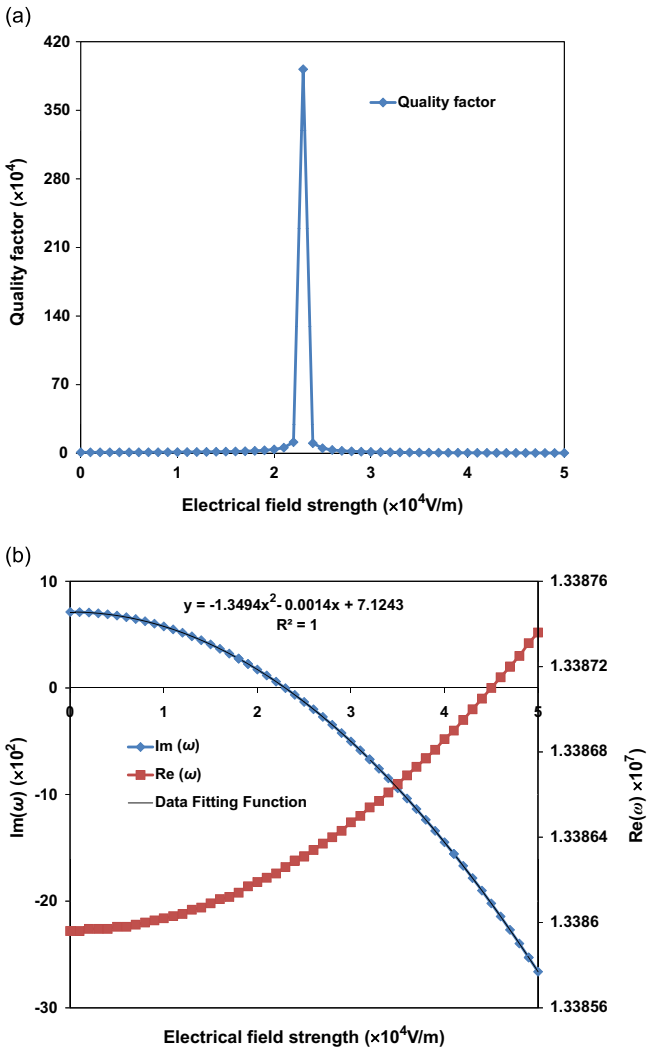

Fig. 5. (a) Quality factor, and (b) Re(ω) and Im(ω) as functions of the strength of the electrical field.

same as those used in the previous section. The analysis was performed under the following two conditions: the applied voltage, V_e, was set to (i) 0 V (standard TED) and (ii) 2 V through the beam (i.e. 1 V through the half beam).

The analytical solution [10] of the quality factor for the standard TED problem is 14,646.7 while the numerical analysis yields 14,721.1 by the Q9 elements with a 13×101 finite element mesh (13 nodes along the height and 101 nodes along the length). The error in the numerical result is approximately 0.508 percent compared to the analytical solution. The results of the quality factor along with both Re(ω) and Im(ω) are also shown in Fig. 4 where the applied voltage is set to 2 V. Similar to the convergence test of the power change discussed previously, the Q9 elements show a faster speed of convergence than the Q4 elements. The results using 9 nodes and 13 nodes along the height are noticeably close to each other when Q9 elements are used. To balance the effort of computation and accuracy, the results based on Q9 elements with two different mesh densities have been compared in Table 2. The numerical error shows that the accuracy based on the 9×41 mesh is more favorable in the current study. The analyses involved in the following sections are therefore based on this mesh density alone.

3.3. Parametric studies

3.3.1. Strength of electrostatic field

The quality factors of the beam resonator under different strengths of the electrical field, E_{es11} (E_{es22} is always zero in the present study), are obtained and shown in Fig. 5(a). The geometric parameters and material properties remain the same.

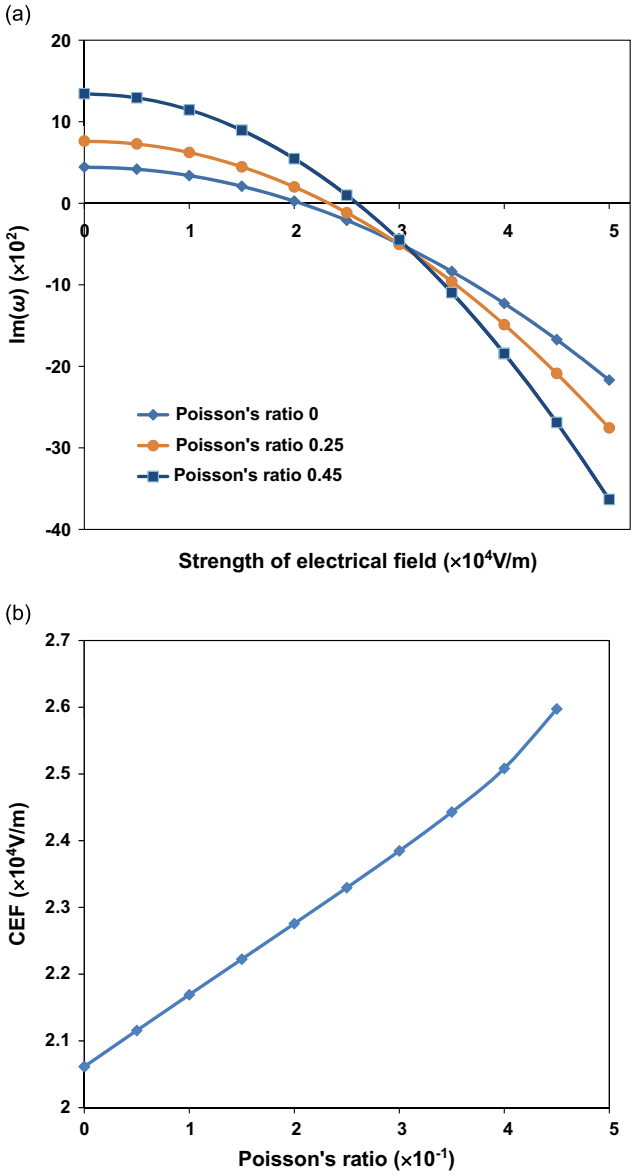

Fig. 6. (a) Im(ω) as a function of the strength of the electrical field and (b) the value of CEF as a function of Poisson's ratio.

A sharp peak is seen in Fig. 5(a) when the electrical field has a strength of 2.3×10^4 V/m. To explain the reason for this peak, the angular frequency of vibration, Re(ω), accompanied by the attenuation, Im(ω), are also presented in Fig. 5(b). It shows that the peak of the quality factor in Fig. 5(a) is caused by the value of Im(ω), which is approaching zero. In addition, Im(ω) decreases with the strength of the electrical field applied on the system. This trend confirms that the electrical field can indeed reduce the energy loss caused by TED.

The regression analysis shows that there exists a strong correlation between Im(ω) and the electrical field since the coefficient of determination is equal to 1. Hence, an interpolating function can be obtained from curve fitting based on a limited number of data points. Furthermore, the fitted function shows that Im(ω) equals zero when the electrical field has a strength of 2.2972×10^4 V/m. According to Eq. (37), in that situation the quality factor approaches infinity and TED is completely compensated by the piezoresistive effect. In the current work we define the strength of the electrical field at zero Im(ω) to be the critical value of the electrical field (CEF). The corresponding applied voltage is denoted as V_{CEF}. The V_{CEF} is obviously the counterpart of the threshold voltage mentioned in Refs. [31,32]. The values of CEF and V_{CEF} are dependent on the beam geometry and material properties.

When the strength of the electrical filed is greater than CEF, Im(ω) will have a negative value. It implies that the change in the electrical power acts as a driving force for the kinetic energy in vibration. By introducing piezoresistivity, the energy loss due to TED can be compensated, leading to a higher quality factor in resonance. Theoretically, the amplitude of vibration

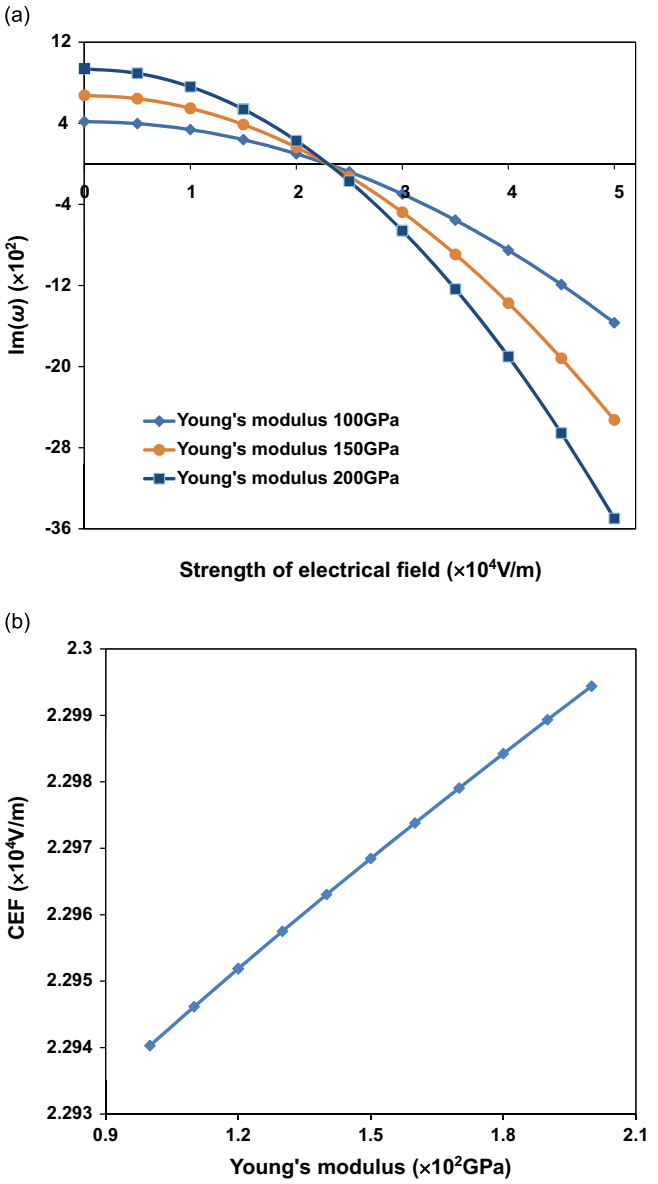

Fig. 7. (a) Im(ω) as a function of the strength of the electrical field and (b) the value of CEF as a function of Young's modulus.

would increase indefinitely, leading to material failure if the system had a sufficiently high input energy. However, in reality the increased vibration amplitude with sufficiently high quality factor will trigger the nonlinear dynamic status of the system [34,35]. The change in the angular frequency Re(ω) as a function of the strength of the electrical field is also shown in Fig. 5(b). Contrary to the result of Im(ω), Re(ω) rises as the electrical field increases its strength. However, the change in Re(ω) is merely 0.001 percent given the present range of the electrical field, which is negligible compared to the change in Im(ω).

3.3.2. Material properties

The parametric study in the following sections is focused on the value of CEF when TED is entirely compensated by the piezoresistive effect. The CEF is estimated from the curving fitting on the results of Im(ω) under the different electrical field strengths. Fig. 6(a) indicates the change in the quality factor as a function of the electrical field strength through the beam for different values of Poisson's ratio. The estimated CEF from curve fitting is shown in Fig. 6(b) as a function of Poisson's ratio. The change is almost linear and the rate is approximately 1.14×10^3 V/m. On the other hand, Fig. 7 shows the effect of Young's modulus when Poisson's ratio is set to 0.22 as denoted in Table 1. Quite different from the effect of Poisson's ratio, when Young's modulus varies, the values of CEF do not differ significantly as seen in Fig. 7(a). However, a more extensive investigation (shown in Fig. 7(b)) has revealed that the change rate of the CEF remains as a linear function of Young's modulus. Nevertheless, such a change rate is only 0.5 V/m/GPa and apparently negligible.

3.3.3. Beam aspect ratio

The studies on the geometric effects are shown in Figs. 8–10. Fig. 8(a) shows the quality factor as a function of the electrical field with different beam lengths while the height, H, is maintained as 10 μm. Fig. 8(b) shows the CEF decreases

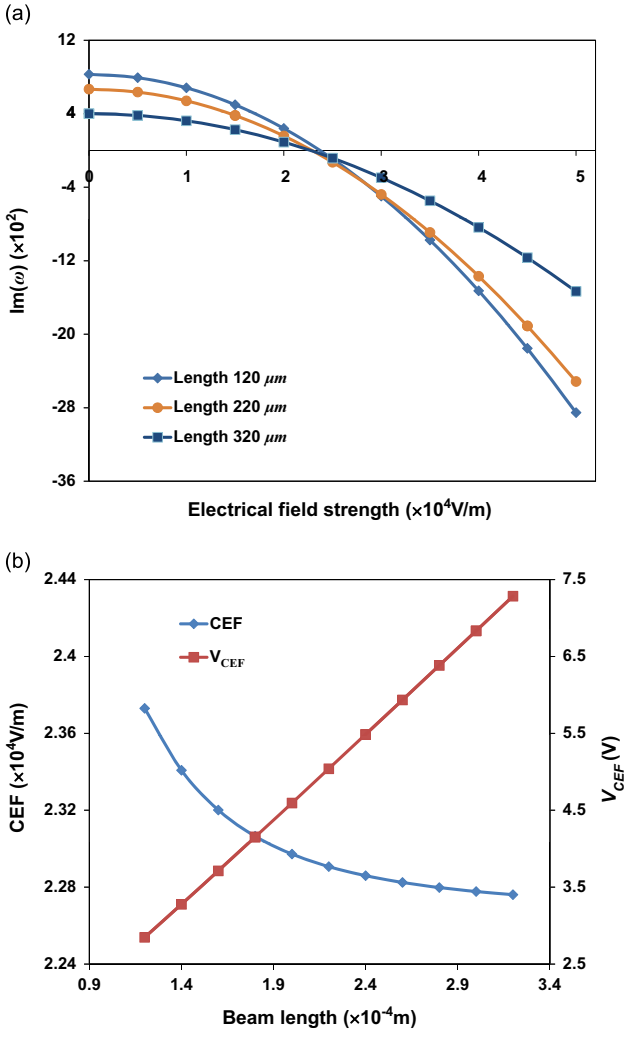

Fig. 8. (a) Im(ω) as a function of the strength of the electrical field and (b) the value of CEF as a function of the beam length.

nonlinearly with the beam length. However, as the length increases by 167 percent from 120 μm to 320 μm, the decrease in the CEF is merely 4.08percent. The V_{CEF} can also be found in Fig. 8(b). Interestingly V_{CEF} increases linearly with the beam length and the rate of the change is approximately 0.022 V/μm. On the other hand, Fig. 9(a) shows the quality factor as a function of the electrical field strength with different heights while the length is maintained as 200 μm. In Fig. 9(b), the CEF is shown as a nonlinear function of the beam height. However, the effect of the beam height on CEF is more significant than the beam length. The CEF decreases by 60.5 percent when the height increases by 166.7 percent from 6 μm to 16 μm. In addition, the V_{CEF} changes in the same trend since the length is maintained constant.

To further study the change in CEF as a function of the beam aspect ratio, $A_r = L/H$, the results in Figs. 8 and 9(b) are reordered and presented in Fig. 10(a). Apparently the CEF changes in opposite directions as the aspect ratio is altered by the length and the height, respectively: The CEF declines nonlinearly with the aspect ratio when the length is changed, meanwhile it increases linearly with the beam aspect ratio when the height is changed and the corresponding rate is approximately 1100 V/m.

Since TED is compensated by the kinetic energy transferred from the input electrical power, there must exist a correlation between the input electrical power, P, and the aspect ratio, A_r. We define the cross-sectional area of the beam as A, and $A = H\delta$ where δ is the beam thickness. Substituting Eqs. (15) into (3), we obtain the input electrical power P_{CEF} as

$$P_{CEF} = \frac{V_{CEF}^2}{R_0} = \frac{V_{CEF}^2 A}{\rho_{es} L} = \frac{V_{CEF}^2 H\delta}{\rho_{es} L} = \frac{V_{CEF}^2 \delta}{\rho_{es} A_r} \tag{38}$$

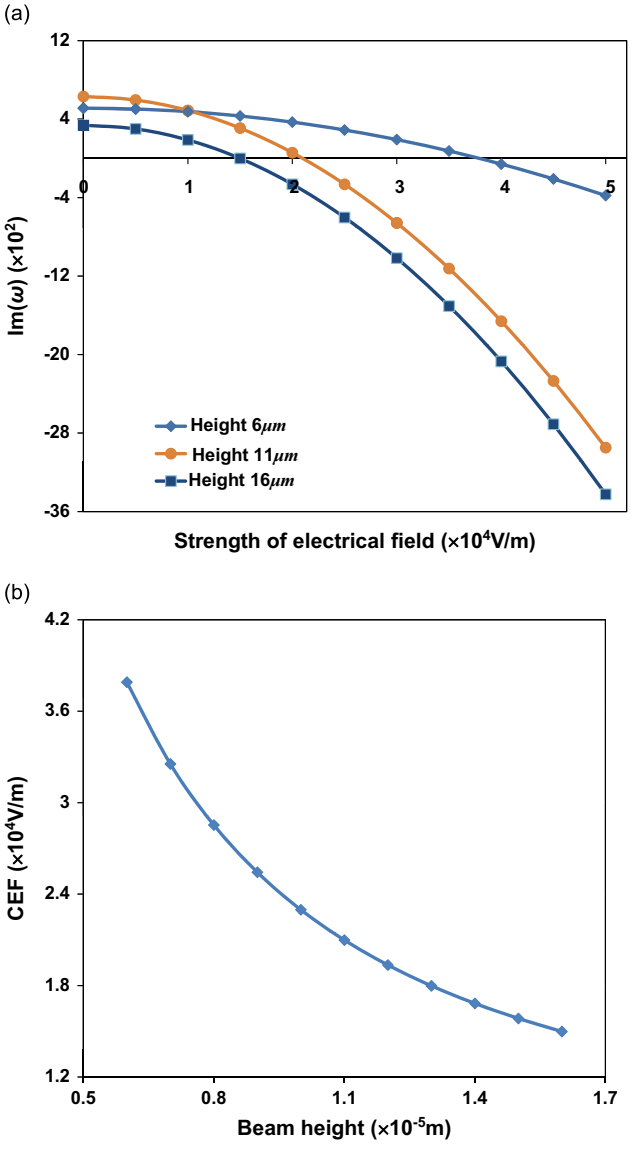

Fig. 9. (a) Im(ω) as a function of the strength of the electrical field and (b) the value of CEF as a function of the beam height.

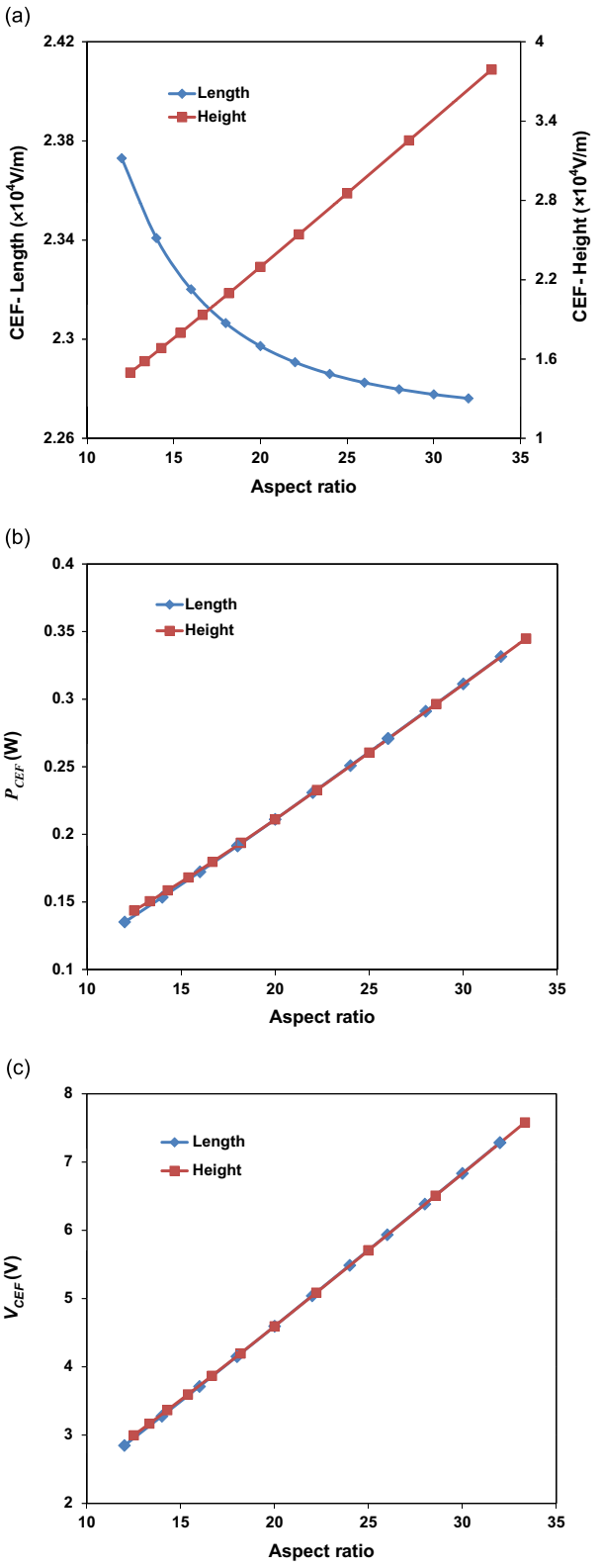

Fig. 10. (a) CEF, (b) P_{CEF} and (c) V_{CEF} as functions of the beam aspect ratio.

The result is presented in Fig. 10(b) and apparently P_{CEF} is a linear function of the beam aspect ratio alone. It indicates that more electrical input power is required to compensate TED when the beam resonator has a greater aspect ratio and the corresponding rate is approximately 0.009 W per unit aspect ratio of beam when the thickness is set to $\delta = 20\,\mu m$.

In addition, for a beam resonator with the same material property and thickness, V_{CEF} is a linear function of the beam aspect ratio alone, as seen in both Eq. (38) and Fig. 10(b). In fact, the slope of the linear regression of the data in Fig. 10(c) indicates that the corresponding rate is approximately 0.22 V per unit aspect ratio of the beam.

3.3.4. Scaling effect

We also investigated the CEF on different size scales toward miniaturization of the beam resonators. Fig. 11(a) shows the result of CEF when the scaling factor of the resonator beam 200 μm × 10 μm changes progressively from × 10,000 (length 2 m, height 0.1 m) to $\times 1 \times 10^{-5}$ (length 2 nm, height 0.1 nm) in a log–log diagram. However, the V_{CEF} has a different trend as shown in Fig. 11(b) since the length here changes differently from the scaling factor. Two distinct plateaus can be seen in Fig.11(b). The first plateau shows the V_{CEF} when the scaling factor is higher than × 100 (length 20 mm, height 1 mm) while

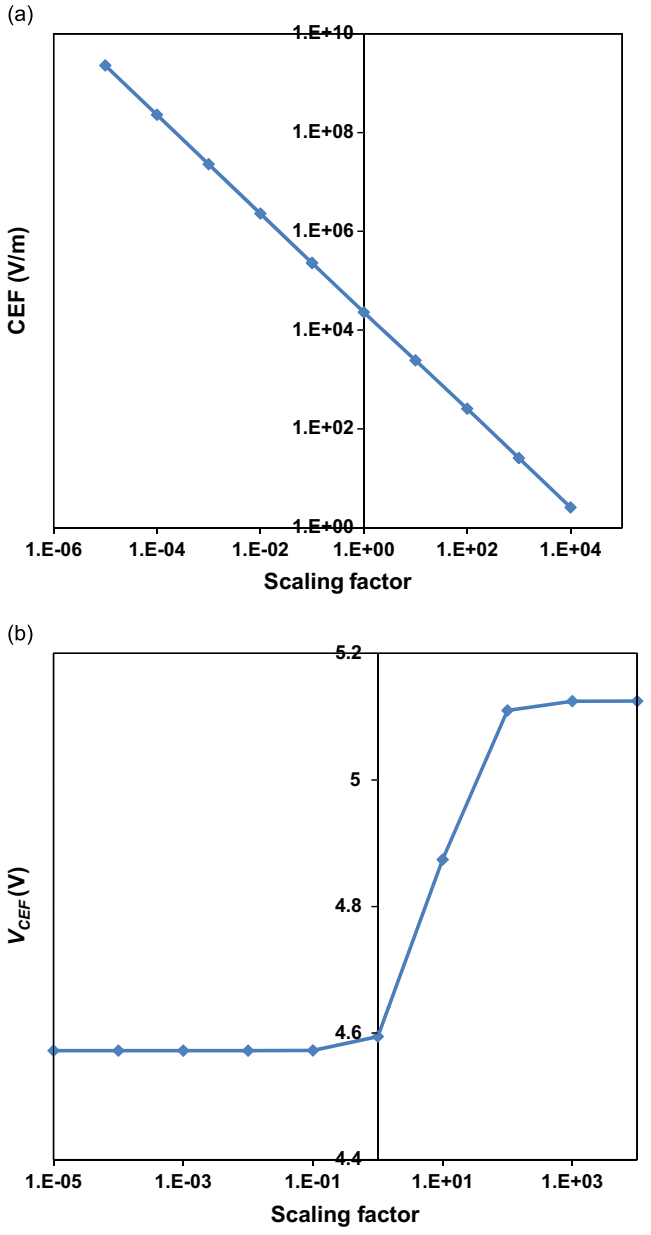

Fig. 11. (a) CEF as a function of the scaling factor of the beam geometry in a log–log plot and (b) V_{CEF} as a function of the scaling factor of the beam geometry.

the second plateau emerges when the scaling factor is lower than $\times 1$ (length 200 μm, height 10 μm). Moreover, the change in the V_{CEF} from the higher plateau to the lower plateau is only about 10 percent from 5.12 V to 4.60 V, meanwhile the size changes dramatically from the meter scale to the nanometer scale.

4. Conclusions

The current work presents a method to enhance the quality factor of MEMS beam resonators vibrating in their flexural modes by applying an electrostatic field on the system with a negative piezoresistive coefficient. During the vibration, the temperature distribution caused by the electrical power change can attenuate the thermoelastic temperature difference that leads to the conductive heat flow from TED. To predict the thermomechanical responses of the system in the presence of piezoresistivity, a set of coupled differential equations for the relevant thermal, mechanical and electrical processes are constructed. These equations are then solved by the Galerkin finite element method. The quality factor is evaluated by an eigenvalue analysis.

A series of convergence studies have been performed using both linear and nonlinear interpolating functions in the finite element method for achieving better accuracy and less computational effort. The quality factor is computed as a function of the strength of the electrical field. The result demonstrates that the quality factor increases with the electrical field strength. Further analysis reveals that an infinite quality factor is possible when the attenuation of vibration, $\mathrm{Im}(\omega)$, equals zero, i.e. TED is completely suppressed. The study also shows that the relationship between the attenuation in the energy loss and the electrical field strength can be presented by a mathematical function from curve fitting. Such a function is also implemented to estimate the value of CEF.

In addition, other parametric studies have indicated the impacts of a variety of material properties and geometric parameters on the CEF and V_{CEF}. For example, the CEF increases linearly with Poisson's ratio whereas Young's modulus has a negligible effect. It has also been found that P_{CEF} and V_{CEF} are functions of the beam aspect ratio alone. On the other hand, the CEF changes linearly with the scaling factor of the miniature model in a log–log diagram, meanwhile there exist two distinct plateaus of CEF in the plot as a function of V_{CEF}.

References

[1] M.F. Zaman, A. Sharma, Z. Hao, F. Ayazi, A mode-matched silicon-yaw tuning-fork gyroscope with subdegree-per-hour allan deviation bias instability, *Journal of Microelectromechanical Systems* 17 (6) (2008) 1526–1536.
[2] C. Comi, A. Corigliano, G. Langfelder, A. Longoni, A. Tocchio, B. Simoni, A resonant microaccelerometer with high sensitivity operating in an oscillating circuit, *Journal of Microelectromechanical Systems* 19 (5) (2010) 1140–1152.
[3] R.A. Barton, B. Ilic, S.S. Verbridge, B.R. Cipriany, J.M. Parpia, H.G. Craighead, Fabrication of a nanomechanical mass sensor containing a nanofluidic channel, *Nano Letters* 10 (6) (2010) 2058–2063.
[4] C.T.C. Nguyen, MEMS technology for timing and frequency control, *IEEE Transactions on Ultrasonics, Ferroelectrics and Frequency Control* 54 (2) (2007) 251–270.
[5] J.T.M. van Beek, R. Puers, A review of MEMS oscillators for frequency reference and timing applications, *Journal of Micromechanics and Microengineering* 22 (1) (2011) 013001.
[6] Z. Hao, E. Ahmet, A. Farrokh, An analytical model for support loss in micromachined beam resonators with in-plane flexural vibrations, *Sensors and Actuators A: Physical* 109 (1) (2003) 156–164.
[7] D. Bindel, S. Govindjee, Elastic PMLs for resonator anchor loss simulation, *International Journal for Numerical Methods in Engineering* 64 (6) (2005) 789–818.
[8] C. Zener, Internal friction in solids. I. Theory of internal friction in reeds, *Physical Review* 52 (3) (1937) 230–235.
[9] C. Zener, Internal friction in solids II. General theory of thermoelastic internal friction, *Physical Review* 53 (1) (1938) 90–99.
[10] R. Lifshitz, M.L. Roukes, Thermoelastic damping in micro-and nanomechanical systems, *Physical Review B* 61 (8) (2000) 5600–5609.
[11] S. Prabhakar, V. Srikar, Theory of thermoelastic damping in micromechanical resonators with two-dimensional heat conduction, *Journal of Microelectromechanical Systems* 17 (2) (2008) 494–502.
[12] S. Prabhakar, M.P. Païdoussis, S. Vengallatore, Analysis of frequency shifts due to thermoelastic coupling in flexural-mode micromechanical and nanomechanical resonators, *Journal of Sound and Vibration* 323 (1) (2009) 385–396.
[13] S.J. Wong, C.H.J. Fox, S. McWilliam, Thermoelastic damping of the in-plane vibration of thin silicon rings, *Journal of Sound and Vibration* 293 (1) (2006) 266–285.
[14] Z. Hao, Thermoelastic damping in the contour-mode vibrations of micro-and nano-electromechanical circular thin-plate resonators, *Journal of Sound and Vibration* 313 (1) (2008) 77–96.
[15] Y. Sun, T. Hironori, Thermoelastic damping of the axisymmetric vibration of circular plate resonators, *Journal of Sound and Vibration* 319 (1) (2009) 392–405.
[16] Y. Sun, S. Masumi, Thermoelastic damping in micro-scale circular plate resonators, *Journal of Sound and Vibration* 329 (3) (2010) 328–337.
[17] M. Zamanian, S.E. Khadem, Analysis of thermoelastic damping in microresonators by considering the stretching effect, *International Journal of Mechanical Sciences* 52 (10) (2010) 1366–1375.
[18] A.R. Vahdat, R. Ghader, Effects of axial and residual stresses on thermoelastic damping in capacitive micro-beam resonators, *Journal of the Franklin Institute* 348 (4) (2011) 622–639.
[19] S.B. Kim, J.H. Kim, Quality factors for the nano-mechanical tubes with thermoelastic damping and initial stress, *Journal of Sound and Vibration* 330 (7) (2011) 1393–1402.
[20] K. Tunvir, C.Q. Ru, A. Mioduchowski, Large-deflection effect on thermoelastic dissipation of microbeam resonators, *Journal of Thermal Stresses* 35 (12) (2012) 1076–1094.
[21] S. Vengallatore, Analysis of thermoelastic damping in laminated composite micromechanical beam resonators, *Journal of Micromechanics and Microengineering* 15 (12) (2005) 2398.
[22] S. Prabhakar, S. Vengallatore, Thermoelastic damping in bilayered micromechanical beam resonators, *Journal of Micromechanics and Microengineering* 17 (3) (2007) 532.
[23] M.J. Silver, L.D. Peterson, R.S. Erwin, Predictive elastothermodynamic damping in finite element models using a perturbation formulation, *AIAA Journal* 43 (12) (2005) 2646–2653.

[24] R.N. Candler, A. Duwel, M. Varghese, S. Chandorkar, M. Hopcroft, W.T. Park, B. Kim, G. Yama, A. Partridge, M. Lutz, T.W. Kenny, Impact of geometry on thermoelastic dissipation in micromechanical resonant beams, *Journal of Microelectromechanical Systems* 15 (4) (2006) 927–934.
[25] Y.B. Yi, Geometric effects on thermoelastic damping in MEMS resonators, *Journal of Sound and Vibration* 309 (3) (2008) 588–599.
[26] Y.B. Yi, Finite element analysis of thermoelastic damping in contour-mode vibrations of micro-and nanoscale ring, disk, and elliptical plate resonators., *ASME Journal of Vibration and Acoustics* 132 (4) (2010) 41015.
[27] X. Guo, Y.B. Yi, S. Pourkamali, A finite element analysis of thermoelastic damping in vented MEMS beam resonators, *International Journal of Mechanical Science* 74 (2013) 73–82.
[28] Y.B. Yi, A. Rahafrooz, S. Pourkamali, Modeling and testing of the collective effects of thermoelastic and fluid damping on silicon MEMS resonators, *Journal of Micro/Nanolithography, MEMS, and MOEMS* 8 (2) (2009) 023010.
[29] S. Pourkamali, A. Hashimura, R. Abdolvand, G.K. Ho, A. Erbil, F. Ayazi, High-Q single crystal silicon HARPSS capacitive beam resonators with self-aligned sub-100-nm transduction gaps, *Journal of Microelectromechanical Systems* 12 (4) (2003) 487–496.
[30] S. Pourkamali, Z. Hao, A. Farrokh, VHF single crystal silicon capacitive elliptic bulk-mode disk resonators—Part II: implementation and characterization, *Journal of Microelectromechanical Systems* 13 (6) (2004) 1054–1062.
[31] K.L. Phan, P.G. Steeneken, M.J. Goossens, G.E.J. Koops, G.J.A.M. Verheijden, J.T.M. van Beek, Spontaneous mechanical oscillation of a DC driven single crystal (2009). *Nature Physics*, 2011, http://dx.doi.org/10.1038/NPHYS1871.
[32] P.G. Steeneken, K.L. Phan, M.J. Goossens, G.E.J. Koops, G.J.A.M. Brom, C. van der Avoort, J.T.M. van Beek, Piezoresistive heat engine and refrigerator, *Nature Physics* 7 (4) (2011) 354–359.
[33] C.S. Smith, Piezoresistance effect in germanium and silicon, *Physical Review* 94 (1) (1954) 42–49.
[34] N. Kacem, S. Hentz, D. Pinto, B. Reig, V. Nguyen, Nonlinear dynamics of nanomechanical beam resonators: improving the performance of NEMS-based sensors, *Nanotechnology* 20 (27) (2009) 275501.
[35] N. Kacem, S. Baguet, S. Hentz, R. Dufour, Computational and quasi-analytical models for non-linear vibrations of resonant MEMS and NEMS sensors, *International Journal of NonLinear Mechanics* 46 (3) (2011) 532–542.